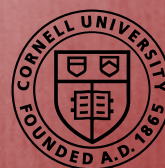




# **REU PROGRAM IN INTERDISCIPLINARY MATERIALS RESEARCH**

Research Reports by Students Supported by  
Cornell Center for Materials Research  
(NSF MRSEC Program, DMR-1719875)

This REU Program for Interdisciplinary Materials Research is co-organized and co-supported by the REU Site for Interdisciplinary Materials Science (NSF REU Site Program, DMR-1757420) and the Cornell Center for Materials Research (NSF MRSEC program, DMR-1719875). This document contains the reports by all students that were funded by CCMR.



# TABLE OF CONTENTS

Student	Faculty Advisor	Page
• Jess Chisholm	• Prof. Zhiting Tian	• 1
• Angelique Miane	• Prof. Atieh Moridi	• 4
• Alison Park	• Prof. Andrew Musser	• 9
• Trine Quady	• Prof. Robert DiStasio Jr.	• 13
• Ron Volkovinsky	• Prof. Carl Franck	• 18

# Towards measuring thin-film aluminium nitride thermal conductivity with frequency domain thermo-reflectance

Jess Chisholm<sup>1</sup>, Zhiting Tian<sup>2</sup>, Gustavo Alvarez Escalante<sup>2</sup>

<sup>1</sup>*Department of Physics, University of Pittsburgh, Pittsburgh PA, USA*

<sup>2</sup>*Sibley School of Mechanical and Aerospace Engineering, Cornell University, Ithaca NY, USA*

(Dated: August 11, 2021)

Understanding the properties of materials is important for reliably and accurately engineering technology. In cases with high heat stress, the thermal conductivities are an important property of potential materials. This is especially relevant for electrical engineering. Frequency domain thermal reflectance, or FDTR, is a method for determining the thermal conductivities of materials. This works by thermally pumping a sample with a laser beam of modulated intensity. The frequency of the pump beam is changed, relating to the depth of heating in the sample. The phase shift of a reflected probe beam is measured, leading to a graph of phase shift and frequency that can be used to determine the thermal conductivity. FDTR relies on a fine-tuned optical alignment which prioritises minimal noise and no overheating. In this paper various methods to ensure that the FDTR setup is reading accurate thermal conductivities will be discussed, along with how to appropriately analyse thermal conductivities from the resulting measurements. Finally, after obtaining accurate results of the thermal conductivity of epitaxy grown AlN, there will be an exploration of the relation of the thermal conductivity and the thickness of the sample.

## I. INTRODUCTION

The thermal conductivity of a material is defined as its ability to transfer heat. A sample (such as silica) which has a low thermal conductivity, optimally conducts heat from one place to another. On the other hand, a high conductivity sample (such as silicon) will show a resistance to thermal energy. Materials of high conductivity are more useful in electronic components where overheating presents a problem. As technology seeks to create the same components with decreasing size, the thermal conductivity of a thin-film sample is important. Non-invasive measure of the thermal conductivity of nano-thin, or two-dimensional, materials ensures that these materials are not damaged. In this way, FDTR is useful for measuring the thermal conductivity for a wide variety of thin film samples—such as Aluminium Nitride.

Frequency domain thermal reflectance works by using the following methods and components. First, there are two lasers of different wavelengths. In the setup used for this paper's results, we use a 532nm green laser and 488nm blue laser as the probe and pump respectively. The pump laser has a modulated intensity such that the intensity is sinusoidal with a frequency which is varied between approximately  $2e4$  and  $2e7$  Hertz. The frequency determines the penetration depth of heating for the sample. For a higher frequency, the penetration depth is small so the probe will measure the phase shift at this point. Whereas, a lower frequency penetrates deeper and will measure the phase shift of a position closer to the substrate. A lock-in amplifier is used to modulate these frequencies accurately. The system focuses both the pump and probe beam towards the sample through an objective. The received phase differences are plotted at modulated frequencies and fitted to determine the thermal conductivity of certain layers.

Samples used in this setup have a collection of un-

known and known values. Of these samples, usually between three and five layers, most of the relevant quantities (thickness, thermal conductivity) should be known. By knowing these values to a reasonable degree, the data can be fitted to find a more reliable value for the unknowns through Fourier analysis and the heat equation. Different unknown attributes have different sensitivities to the frequency of the modulated laser. In the case for Aluminium Nitride samples, the interfacial thermal conductivities and the thermal conductivity of the thin-film are fitted with non-linear least squares for two of the three parameters through several rotations until consistent values are reached. The results found later in this paper all use this iterative method. By rotating through two-parameter fits of 3 different combinations for the total of three parameters, a convergence is found regardless of the starting guesses for unknown values.[1]

## II. FDTR SYSTEM AND TROUBLESHOOTING

Optical alignment is important in the FDTR setup. The incident and reflected beams of both the pump and probe laser need to be coaxially aligned for the results to be reliable. If this is not the case, then the sample will not be heated uniformly or in the same position as where the probe is reading the phase shift. To ensure this alignment, the beams should be directed beam through a “mirror maze” or across any sizeable distance. The beams should be checked at several points along this path to check that they do not diverge. Some divergence at large distances would be acceptable, as long as it is reliably coaxial for the optical path length of the system. This is checked for both the incident and reflected beams.

While the optical setup may be almost perfect, another large source of error is the tilt stage for the sample. If the tilt stage is set for one point on a sample, there is

no guarantee that it is zeroed for other positions or for another sample. Zeroing the tilt stage, means ensuring that the interface is exactly perpendicular to the incoming light, allowing the reflected light to return in exactly the same plane. When the tilt stage is at an angle, it leads to a characteristic shifting of low frequency results. While this appears acceptable at higher frequencies, the lower frequency shift can skew the fitted values.

A problem that persisted throughout our earlier experimentation was a clear shift in our results. The graph appeared to be shifted to lower frequencies, showing a good curve but incorrect thermal conductivity when fitted. At first, it appeared that there might be some error with the internal clock of the lock-in amplifier since that would lead to frequencies being displaced consistently. However, it became clear that the problem was over-heating of the sample. Especially for the lower thermal conductivity silica, the problem showed a greater displacement. This led to an extended project investigating the optimum power balance for the pump and probe for high and low thermal conductivity samples.

### A. Balancing Pump Power

For a reference samples of both high and low thermal conductivities, we tested where the value stabilised. It was found that the thermal conductivity was more affected by the pump laser than by the probe laser. This was expected, since the pump is what is heating the sample. For lower thermal conductivities it's intuitive that this value should be low so the sample does not experience overheating that will skew the results. For higher thermal conductivities it will need to be higher.

In Fig. 1, shown are the results of power analysis for a gold on silica sample. A small window was tested thoroughly to find the most stable point for future measurements. This included balancing the overheating that occurred with higher powers against the noise that is introduced with lower powers. The resulting minimum of 11mW is now used for low thermal conductivity samples, with a fixed high probe power of 0.04W. The probe power should be kept as high as it can without damaging the photodiode so to maximise the signal to noise ratio.

Following this, a higher thermal conductivity reference sample was tested, giving a much higher optimal pump power. Higher thermal conductivities are not so drastically affected by overheating, leading to a greater range of acceptability around 70mW for thermal conductivities of approximately 100-200W m<sup>-1</sup> K<sup>-1</sup> and 100mW for 200-300W m<sup>-1</sup> K<sup>-1</sup>. As a result of troubleshooting and the power balancing analysis, our results become more consistently reliable. In any case, the project that I was initially meant to work on involved measuring the thermal conductivities of AlN samples with differing thicknesses. After finding that we can get reasonably accurate results after two months of troubleshooting, it's time for some initial data. .

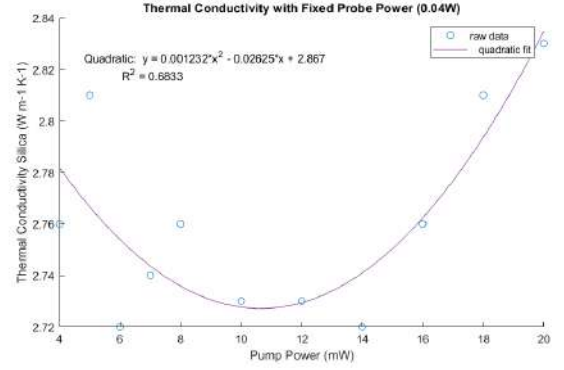


FIG. 1. Measured thermal conductivity with varying powers of the pump laser. This shows a range of overheating that occurs at higher powers, and an increase of noise at the lower powers. The optimum power value is found as the minimum of the quadratic which gives 11mW. The stability of this value was tested, showing reliably consistent results within a percent of error.

## III. RESULTS AND ANALYSIS: EPITAXIAL ALN THERMAL CONDUCTIVITY

The AlN (thin-film Aluminium Nitride) samples are grown with three layers. The substrate is bulk AlN, while the middle layer is epitaxial grown AlN of a certain thickness, and the top layer is gold. The matrix representing known and unknown values for the full sample thus has five rows: three for the layers, and two for the interfaces. The interface between bulk AlN and epitaxial grown AlN is very large while the interface between epitaxial grown AlN and Au is lower (yet still high). This is because thermal conductivity is more efficient between two layers of the same type of material. Results were taken for a range of epitaxial grown AlN thicknesses between 100nm and 3μm.

Sensitivity analysis determines how sensitive the phase difference is to the value of the unknown parameter-this is shown in Fig 2. In the case of AlN, this gives a general trend of rising sensitivity for the thermal conductivity of the epitaxial layer for a larger thickness. On the other hand, the interfacial thermal conductivity between the bulk AlN and epitaxial AlN has a generally decreasing phase sensitivity for larger thicknesses. However, these parameters are all unknown and are treated similarly important in the fitting method. We have a good estimate of the thermal conductivity of the AlN samples which dictates our initial guess. Both interfacial values are simultaneously fit through an initial iterations, then the first interface and the epitaxial AlN is fitted, and finally the second interface and epitaxial AlN. This is repeated through over twenty cycles to eventually reach a converged result which is recorded. The thicker the sample, the closer the thermal conductivity tends towards the value for bulk. The converged values are consistent despite the initial guesses for the unknown values.



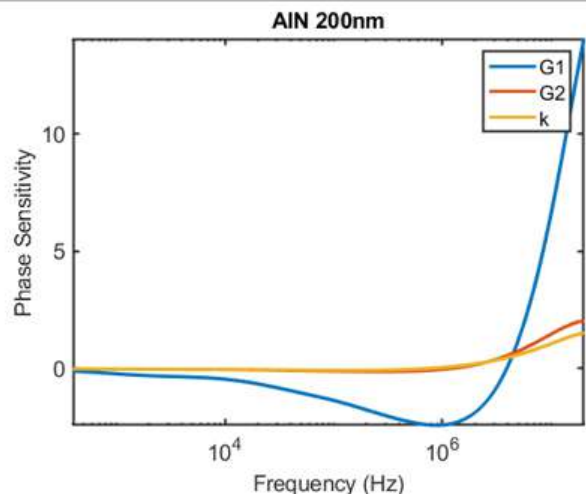


FIG. 2. Sensitivity analysis of the unknown parameters of the 200nm epitaxial AlN sample shows that the interfacial thermal conductance of both interfaces (G1 for gold-eAlN; G2 for eAlN-bulk AlN) and the thermal conductance of the epitaxial layer (k) are relevant through the frequency range. While being more sensitive at higher frequencies, a balanced approach to fitting the data allows for the unknowns to slowly converge to a point where they are each consistent in relation to each other. At this point, which is reached regardless of initial estimates, the data is optimally fitted. The sensitivity analysis confirms that this is an important method for fitting the data since each unknown is similarly sensitive.

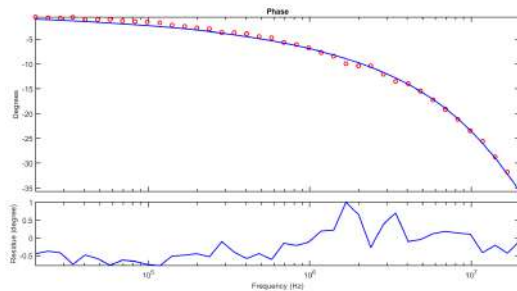


FIG. 3. For a sample of Gold on 200nm Epitaxial grown AlN on AlN bulk, we used FDTR to determine the thermal conductivity. The raw data is in red while the best fit is the optical alignment is shown to be near-perfect as the noise profile of the data is not significant. When the alignment is not fixed, lower frequency results drift up while characteristic spikes appear at mid-high frequencies. The residue of the data is the difference between the raw data and the expected data according to the fitted curve. For this average of three runs, the calculated thermal conductivity of the thin-layer AlN was 65.8 W m<sup>-1</sup> K<sup>-1</sup>.

Fig. 3 shows our current data for the 200nm sample. This will be repeated at least six times so that an average thermal conductivity can be found. The thermal conductivity of all other thicknesses will be found to realise the relation between thickness and thermal conductivity. The focus on alignment and data analysis has improved upon our initial results that had a high level of noise and a large divergence from expected values.

#### IV. CONCLUSION

The thermal conductivity of thin film samples can be determined through frequency domain thermoreflectance. This method involves modulating a pump laser with a frequency that is inversely proportional to the depth penetrated. The second laser, the probe, then determines the phase shift at this point. Using known and estimated quantities, the data can then be fitted with some degree of accuracy. The accuracy increases with an increasing number of iterations. However, the iterations should focus first on the most sensitive parameters. After rotating through these iterations several times, the unknowns will converge into a consistent result regardless of the initial values. Using this method, we find the thermal conductance of a 200nm AlN sample near the theoretical expectations. Finding these values accurately is important for these materials since Aluminium Nitride is a large thermal conductivity material. AlN can be epitaxially grown in thin films while retaining a relatively high thermal conductivity that tends towards 321 W m<sup>-1</sup> K<sup>-1</sup> for larger thicknesses. This is useful in electrical components where there will be a high level of heating. In conclusion, FDTR is a good method of determining thermal conductivities for nanofilms and AlN is a promising material for high thermal conductivity requirements.

#### ACKNOWLEDGMENTS

Thanks to CCMR for running this program and NSF for funding it. With the guidance of Gustavo Alvarez Escalante and professor Zhiting Tian, I gained valuable experience that has made this paper possible.

[1] J. Yang, "Thermal property measurement with frequency domain thermoreflectance," <https://open.bu.edu/handle/2144/17057>, dissertation; 2016.

# Observations of Particle Impact During Directed Energy Deposition

Angelique Jan Miane<sup>1</sup>, Adrita Dass<sup>2</sup>, Niharika Shukla<sup>2</sup>, and Atieh Moridi<sup>2</sup>

<sup>1</sup>*Department of Mechanical and Aerospace Engineering, University at Buffalo, Buffalo NY, USA 14260*

<sup>2</sup>*Sibley School of Mechanical and Aerospace Engineering, Cornell University, Ithaca NY, USA 14853*

(Dated: August 11, 2021)

Additive manufacturing (AM) has gained popularity over the last decade as a manufacturing technique. Without the need of traditional machining methods, this technique has the ability to create complex structures and shapes. One type of AM, laser directed energy deposition (L-DED), is emerging to be a new wave of manufacturing by having the potential to print metals and alloy systems. We aim to understand the interactions of the metal particle interactions with the melt pool in order to determine major parameters/factors of the process. Consequently, the new information obtained would serve as the basis for further research in overcoming prominent challenges with L-DED. This paper provides the methodology of developing a nozzle apparatus to better understand these interactions. Trial and error has resulted in predicting that the certain model created could be improved through a single-part design rather than a multi-part one. Also, the trajectory of the powder particles can be further analyzed with a simpler nozzle model to study this particular parameter.

## I. INTRODUCTION

Additive manufacturing (AM) is the creation of three-dimensional objects by “printing” materials, such as plastic or metal, layer by layer. Commonly known as 3D printing, this manufacturing technique has the ability to produce sophisticated work without using traditional machining methods. This paper specifically focuses on laser directed energy deposition (L-DED), a type of AM that prints metals (and alloy systems) with a laser beam as its heat source. Metallic powders are fed into a powder hopper and proceed to a nozzle where they are then ejected using pressurized inert carrier gas. As shown in Fig. 1, the ejected particles travel towards a substrate and melted by the laser beam at a common point of trajectory. The melted powders then create a melt pool that forms a layer on the substrate surface.

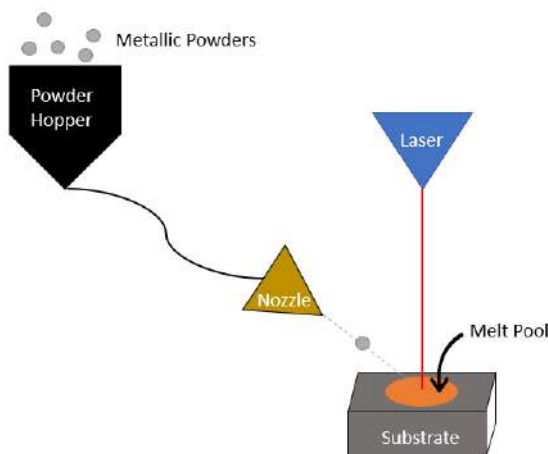


FIG. 1. Simplified L-DED Process

L-DED has the potential to be applicable in a variety of industries such as biomedical, welding and cladding, repair,

bulk combinatorial alloy design, construction materials, and hybrid additive manufacturing [2]. Although L-DED presents numerous applications, challenges prevent this technique from being commonly used. Due to the random and unknown nature of particle interactions with the dynamic melt pool, printed parts have inhomogeneous structure and properties. This creates poor repeatability. Furthermore, the past work of Haley et. al has documented that there is a low powder capture efficiency with the L-DED process[1]. It was shown that particles tend to impact and float on the melt pool surface before subsuming below. During this time period (of hundreds of microseconds), incoming particles are shielded from being melted by rebounding off its floating counterparts. The challenges of L-DED can be strongly attributed to the fact that the correlation of process parameters (like powder impact velocity, particle residence time, nozzle geometry and so on) and the interactions of powder particles in the melt pool are poorly understood. We seek to determine these particular major parameters/factors that impact the interactions between powder particles and the melt pool during L-DED. In order to do so, we need to study the interaction of a single powder particle with the melt pool at a time. It is easier to track and observe a single particle-melt pool interaction rather than a cluster of particles. This paper discusses the development of a nozzle and experimental apparatus to feed micro-sized powder particles one at a time to achieve this feat. Through this, we hope to better understand the precise workings of the L-DED process and its parameters.

## II. MATERIALS AND METHODS

### A. Apparatus Set-Up

The L-DED lab set-up is shown below in Fig. 2. The laser is controlled remotely via a laptop and computer system. The printing enclosure is highlighted and has

an approximately 38 cm sized hole at the side to insert nozzle configuration.

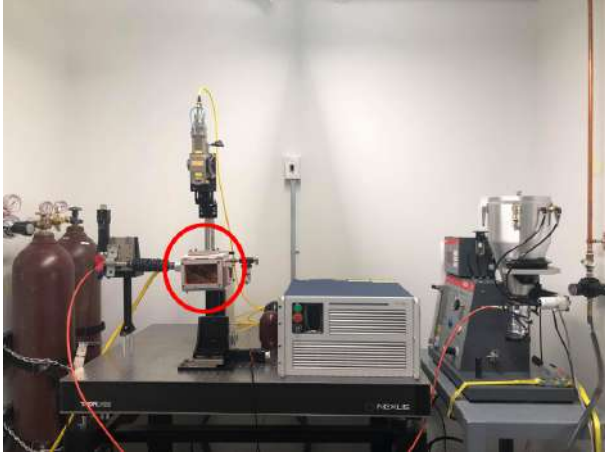


FIG. 2. L-DED Set-Up

First, a computer-aided design (CAD) of an initial model was drafted. The design consisted of a powder hopper (1), spring-loaded valve (2), a threaded connector pipe (3), a plastic threaded adapter (4), three-way distillation adapter (5), a glass vacuum adapter straight with a 24/40 outer joint (6), a glass vacuum adapter straight with a 24/40 inner joint (7), and a 0.16 mm glass capillary (8). Fig. 3 shows the described model below.

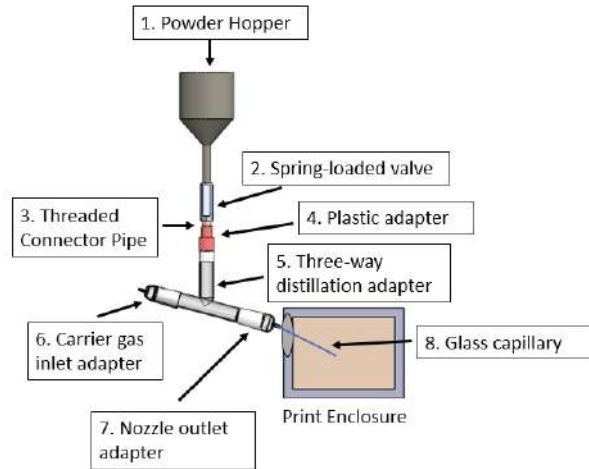


FIG. 3. Initial Nozzle Apparatus Model

Not labelled is the small piece of a rubber stopper that was cut out to fit into the nozzle outlet adapter opening. A size 1 sewing needle was pierced through the middle of the small rubber piece in order to create a small hole to insert the glass capillary. This small rubber piecing was able to seal the vacuum adapter opening in connection to the glass capillary to lessen the amount of air leakage. This specific connection is indicated in Fig. 4.



FIG. 4. Nozzle Adapter and Glass Capillary Connection

In addition to the nozzle apparatus, plumber sealant and Teflon tape were used to seal the threads and connections so that there would be also be lessened air leakage. A no.8 rubber stopper was also used to seal the printing enclosure hole to steady the apparatus when in use.

When test running the initial design with pressurized air, the nozzle outlet adapter flew off the apparatus due to air escaping through its connection with the three-way distillation adapter. This meant that the plumber sealant was not enough to hold it in place, and thus black electrical tape was wrapped around the 24/40 inner joint to fill in the connection gap. The tape was then used to reinforce the separated connection to stop the air from leaking through it, and to stop the adapter from flying off. It was also revealed that the carrier inlet gas adapter of the initial design was incompatible with the pressurized air hose fitting. Fig. 5 showcases that the glass vacuum adapter straight with a 24/40 outer joint was replaced with another threaded connector pipe and plastic threaded adapter set.

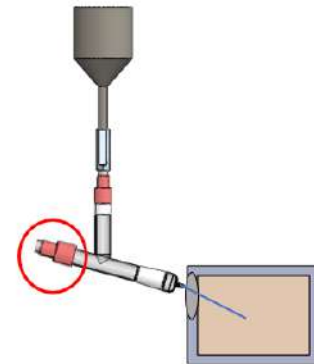


FIG. 5. Modified Nozzle Apparatus Model

The threaded connector pipe was able to screw perfectly into the carrier gas hose fitting. This secondary iteration of the nozzle apparatus was then tested to see if this design was viable to observe the micro particles in action. The assembled model can be seen in Fig. 6 below.



FIG. 6. Assembled Nozzle Apparatus

### B. Experiments

It was decided to use Inconel-625 as the testing powder particles due to its high stability and varied particle size (45 to 150  $\mu\text{m}$ ). Since the glass capillary has a tip size of 160  $\mu\text{m}$ , it was estimated to shoot out individual or small groups of particles at a time. This would make observing the particle-melt pool interactions easier than huge groups coming out.

Prior to using the L-DED set-up, the nozzle apparatus was tested by itself without the requirement of a laser. The apparatus was held up by a support stand and clamp. It was estimated that distance from capillary tip to bottom of printing enclosure would be 5 centimeters and the projected ejection velocity would be 10 meters per second. The calculation below shows that the time it would take a single particle to travel that distance would be 0.005 seconds or 5 milliseconds.

Particle Travel Time

$$= \frac{5 \text{ cm}}{10 \text{ m/s}} = \frac{0.05 \text{ m}}{10 \text{ m/s}} = 0.005 \text{ seconds} = 5 \text{ milliseconds} \quad (1)$$

It was concluded that a recording device would require a frame rate of 200 frames per second (FPS) with the calculation generated below. This frame rate would have the ability to capture the particle at that travel time with the same resulting particle travel time as before.

Particle Travel Time

$$= \frac{1 \text{ second}}{200 \text{ frames}} = 0.005 \text{ seconds} = 5 \text{ milliseconds} \quad (2)$$

Newer iPhone models (8 or greater) can record slo-mo videos at 240 FPS [3]. With the current equipment

at hand, it was decided that an iPhone 8 would be the right choice as a recording device at these experimental stages. It would give us a good indication on the required camera specifications at later stages of the project. The room lights were turned off, a flashlight was shone in the trajectory area, and a dark red backdrop was placed in efforts to make the powder particles exiting the glass capillary more obvious as illustrated below in Fig. 7.



FIG. 7. Dark, Red Background

Test running the modified nozzle apparatus design presented numerous flaws. First, with the pressurized hose inserted into the nozzle system via hose, there were still air leaks arising between the part connections. This would cause a decrease in the final nozzle velocity as there is less force to push the particles through. At higher pressures, there were concerns with parts flying off again. Thus, only 5 PSI was used during these stages. Furthermore, when the valve was open to release the particles from the hopper to the three-way distillation adapter the pressurized air flowed up the valve and hopper. Fluid, such as air, flows from areas with higher energy levels to lower ones. This caused an increase in pressure of the powder hopper, and resulted in the most of the particles unable to flow downward into the three-way adapter. Those that did get stuck in the nozzle adapter due to the larger diameter contrast of the design, and none went through the glass capillary.

After a multitude of thorough test runs, the same overlying problems of the design kept persisting. Thus, we looked toward a simpler model of the proposed set-up. The same dark, red background and flashlight component of the modified design nozzle apparatus was kept. Inconel-625, an iPhone 8 as the recording device and the 5 PSI as the air pressure was also kept constant from the previous methods. However now with the support stand and clamp, the clamp gap was filled in with plumber sealant. Instead of looking at micro-particle and melt pool interactions, we sought to find powder trajectory parameters. A 500  $\mu\text{m}$  glass capillary tip was used instead to ensure the ability to observe the powder trajectory. About 0.001 grams of Inconel-625 particles was meticulously inserted in the capillary tip. Once the glass capillary was placed and set in the plumber sealant, the pressurized air would be pushed through the other end and forced to eject from



the tip, all while being recorded in slow motion with an iPhone 8.

### III. RESULTS AND FUTURE DIRECTIONS

Unfortunately, mixed data was captured with the modified design and thus viable data analysis could not be conducted. However, it can be said that other designs of a nozzle apparatus should be looked at. Instead of having several different parts and causing air leaks through the connections, a single part should act as a nozzle. Possibly, a custom-made device could be modelled and sent out to be built by field experts (depending on the materials decided). Unlike the model discussed in this paper, this singular device would also be smaller in diameter. This would lessen the amount of particle loss as it goes through the apparatus. The proposed single part could also be a powder spray gun, commonly used for powder paints, but the issue of clogging could hinder this method. Having some way to control the powder flow would increase the efficiency of this design. Thus, further research in a unique particle spray apparatus should be looked into.

With the simpler set-up, a cluster of powder trajectories could be observed. Shown in Figure 8 is a still image of powders being ejected from the capillary tip.



FIG. 8. Powder Trajectory of a Simpler Model

Using the program ImageJ, the particles could be placed in a black and white, binary system. Figure 9 illustrates an image of the particle trajectory when processed through ImageJ.

The cluster of white pixels coming from the upper, left corner and diverging outward are the powder particles. They are outlined in a yellow border. For future analysis, the ratio of white pixels over that total amount of pixels (black and white) could be determined in order to see the changing volume of the powder trajectory as it travels further out of the nozzle. Not to mention, by finding the trajectory patterns of the nozzle it would be easier to pinpoint the exact location the cloud of particles would hit on the substrate to increase the particle capture rate of the laser system when printing.

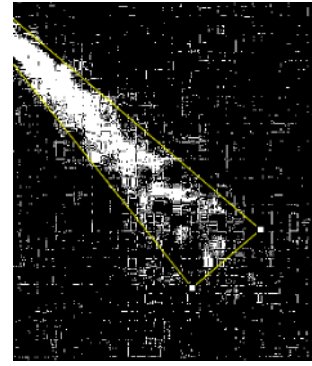


FIG. 9. Powder Trajectory in a Binary System

Additionally, a recording device with a higher magnification specification or a lens system should be considered. Although none of the Inconel-625 particles went through the 160  $\mu\text{m}$  capillary tip for the modified design, the particles stuck in the nozzle adapter were difficult to observe due to their small size. Also, with the simpler model the iPhone 8 camera could not provide enough resolution and contrast. Since it was difficult to eject a single particle, it was difficult to track the particle velocity at such a lower fps. Thus, a higher quality set-up consisting of multiple cameras and lens systems, as demonstrated in Haley 2019, should be given greater attention to look into to give more detailed data[3].

### IV. CONCLUSIONS

Utilizing a nozzle model as seen in Fig. 5 and 6 should be further revised to study micro-particle interactions with the melt pool. It was not able to eject Inconel-625 particles through the 160  $\mu\text{m}$  glass capillary tip due to pressure build up, particle loss, and air leaks. Future work to be considered concerning a single-part device and the recording set-up is highly encouraged. The trajectory of the powders can also be further explored to predict the area of which the powders would impact the substrate in order to possibly increase the powder capture rate. This study could be directly translated to a more advanced and working nozzle model for single particle observations.

### V. ACKNOWLEDGEMENTS

Thank you to the entire Moridi group, especially Professor Atieh Moridi, for giving me this opportunity to grow with this project as well as welcoming me into the laboratory. I give huge thanks to Adrita Dass and Niharika Shukla in guiding me and always helping whenever I needed assistance no matter how busy they were. This work was supported by the Cornell Center for Materials Research with funding from the National Science Foundation.

## VI. REFERENCES

[1]Apple Inc. (2021, April 15). iPhone 8 - Technical Specifications. Retrieved August 6, 2021, from [https://support.apple.com/kb/SP768?locale=en\\_US](https://support.apple.com/kb/SP768?locale=en_US)

[2]Dass, A., Moridi, A. (2019). State of the Art in Directed Energy Deposition: From Additive Manufacturing to Materials Design. THE Coatings, 9, 418.

[3]Haley, James Schoenung, Julie Lavernia, Enrique. (2018). Observations of Particle-Melt Pool Impact Events in Directed Energy Deposition. Additive Manufacturing. 22. 10.1016/j.addma.2018.04.028.

# **Trapping Light to Rewire Organic Semiconductors**

**Alison Park, Scott Renken, Andrew Musser**

## **Abstract**

The phenom of strong exciton-photon coupling in photonic structures results in a quasiparticle known as the polariton. The polariton has still yet to be largely explored for organic materials as previous scientific explorations have focused on inorganic systems. There is a value in exploring organic systems to see how and if polariton behavior differs to better tune their properties for commercial design. Organic polaritons have great potential for applications in carbon-based semiconductors, which see use in solar cells and OLED displays. This paper focuses on optical planar microcavity structures being created to further understand the inducing conditions and energetic behavior of the polariton.

## **Introduction & Background**

The semiconductor industry is present in almost every aspect of the modern-day life and serves as an essential component for all electronic devices. They are the centripetal force for means of communication, computing, healthcare, and transportation by providing the ability to control the electrical conductivity within devices in the solid state. The current forefront semiconductor materials are silicon, germanium, and gallium arsenide. Of these, silicon is most notable for its low raw cost, ease in doping processing, and effective temperature range. Recent research pursuits, however, have discovered that certain organic materials can provide similar functions to silicon semiconductors.

Organic semiconductors do not have to be based on a rigid substrate structure as their inorganic counterparts. Thus, organic materials can provide a much more flexible use in their mechanical design while also having the added benefit of being a significantly more affordable product. The large limiting factor remains to be that the current energetic efficiencies of silicon semiconductors still outweigh that of organics. Although, carbon-based organic

semiconductors have seen some success in developing processing means that find planes of conductivity.

Strong light-matter coupling can rearrange the exciton energies in organic semiconductors (2). And when the cavity mode exists at the same wavelength as the last absorption peak of the organic material, a quasi-particle called a polariton will form. The existence of the polariton allows for the organic material to have a new absorbance state at lower energies, which be beneficial in the design for future electronic devices.

There is still much to be learned about the properties of organic semiconductors. To simulate and better understand their functional behavior, optical planar microcavities can be constructed. The cavities can then be studied by employing light spectroscopy techniques.

A planar microcavity is comprised of two mirrors that are separated by a certain thickness 'L' and within this region the organic material is placed. Commonly, metallic films or dielectric distributed Bragg reflectors (DBRs) are used for the microcavity's mirrors. DBRs are designed with alternating layers of transparent materials with high and low refractive indices. These layers create a highly

reflective structure, as opposed to the typical optical absorption loss metallic mirrors face (1). Thus, DBRs are often preferred over metallic mirrors.

## Experimental Section

### Microcavity Construction

A hybrid metal-DBR cavity was prepared using an electron-beam evaporation sputtering technique and measured using a profilometer. The DBR consisted of alternating TiO<sub>2</sub> and SiO<sub>2</sub> layers, with their planned and observed thicknesses noted in Table 1. A silver layer of 30 nm was deposited as the cavity's uppermost layer and this thickness was confirmed by the evaporator's profilometer. While the DBR has a higher Q-factor and provides for greater absorption, it requires a significant amount of processing (roughly 16 continuous hours for the DBR deposition described). The DBR is also not a removable layer as opposed to the silver. Thus, as a matter of convenience in aspects of time and labor, a hybrid construction was chosen.

**Table 1:** DBR Planned and Observed Thickness

Layer *	Planned Thickness (Angstroms)	Observed Thickness (Angstroms)
TiO <sub>2</sub>	507	507
SiO <sub>2</sub>	751	751
TiO <sub>2</sub>	507	507
SiO <sub>2</sub>	751	751
TiO <sub>2</sub>	507	507
SiO <sub>2</sub>	751	920
TiO <sub>2</sub>	507	507
SiO <sub>2</sub>	751	751
TiO <sub>2</sub>	507	507
SiO <sub>2</sub>	751	751
TiO <sub>2</sub>	507	507

\*Reads bottom (first deposition) to top (last deposition)

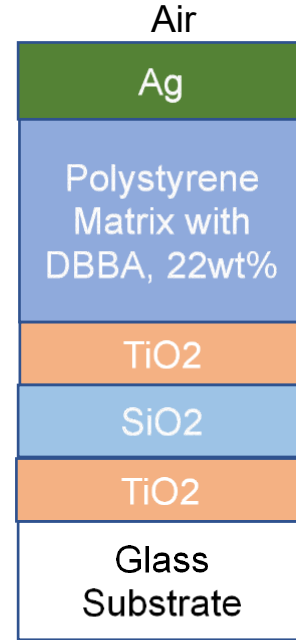


**Figure 1:** Hybrid Metal-DBR cavity construction

### Organic Layer

DBBA-Anthracene was chosen for it being an organic material that is a strong absorber and for already having previously published success of displaying a strong coupling regime. Multiple microcavities of varying concentrations and thicknesses of the organic layer were created. The attempted concentrations include 6.25wt%, 12.5wt%, 22wt%, and 50wt%. Toluene was used as the solvent.

To deem the most successful coupling regime, the cavities were then analyzed by using their angle dependent reflectivity measurements to plot heat maps. These plots of wavelength vs angle provide a clear visual of the polariton's presence with the splitting of the absorption peak.

### Physical and Theoretical Verification

To verify the physical thickness of the organic layer, a MircoMechanical Analyzer was used on a 'blank' cavity—



cavity without the organic material in the polystyrene matrix. The ‘blank’ underwent the same spin coating deposition as the hybrid cavity with the organic material and is expected to return similar values.

In addition, a computational modeling program based on a transfer matrix thin film theory was utilized to theoretically confirm the microcavity’s strong coupling behavior.

## Results and Discussion

The constructed microcavities underwent angle-dependent reflectivity measurements. The resulting data was used to plot a heat map of the reflectivity intensities to visually display any potential polariton behavior. The strongest anti crossing behavior was present for DBBA of 22wt%.

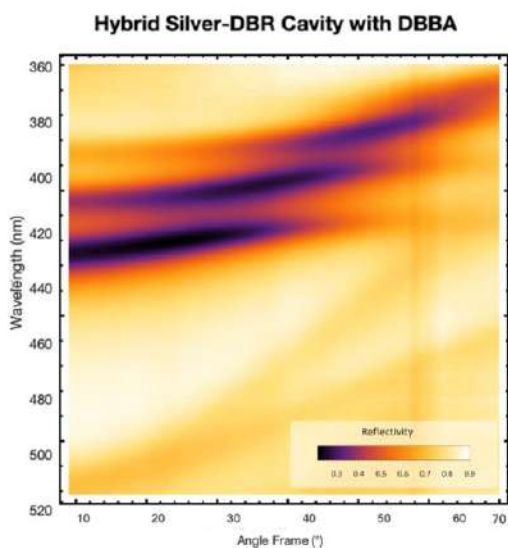


**Figure 2:** Hybrid Metal-DBR Cavity of 22wt% DBBA-Anthracene Reflectivity Map

The drops in reflectivity confirm that the molecule has a new absorption state at a lower energy value.

To further verify polariton’s presence a transfer matrix model was used to simulate the cavity’s expected behavior.

The model is based on a multilayer film theory and parameters such as thickness, exciton wavelength, and index of refraction were inputted to describe the cavity. When the organic layer’s thickness was described as 480 nm, the simulation provided a reflectivity heat map that strongly correlated to the experimental measurements that were taken.

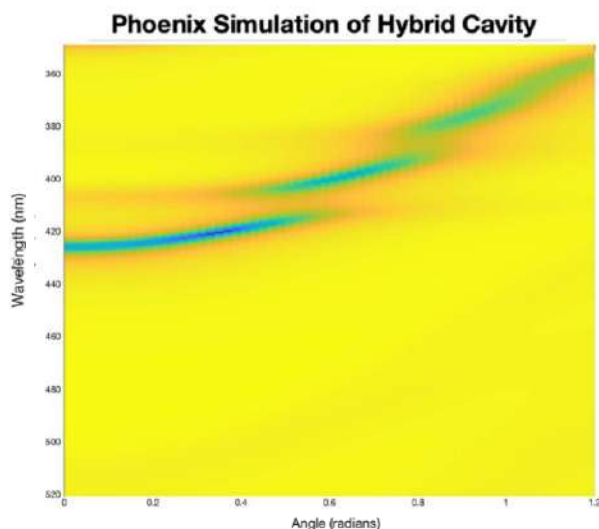


**Figure 3:** Hybrid Cavity Simulation Result for 480 nm

In addition, the micromechanical analyzer described the blank cavity to have a thickness in the range of 510-580 nm.

The theoretical simulation using the transfer matrix and the physical measurement data of the organic layer’s thickness corroborate and suggest that the layer is indeed in the realm of 500 nm. Although this value varies significantly from the intended 162 nm, we can attribute this difference to the inconsistency of the spin-coat method.

## Conclusion

To conclude, 22wt% DBBA-Anthracene in a Toluene solvent was confirmed to show polariton behavior.

While the exact thickness of the constructed microcavity remains to be unable to be fully confirmed, the results suggests that it was around 500 nm.

To further investigate the polariton's behavior, the coupled oscillator method could be explored to better define the energetic behavior. It would also be interesting to pursue time-resolved measurements to create polariton 'movies.'

## Acknowledgements

I would like to thank Professor Andrew Musser for allowing me the opportunity and resources to work in his lab. I was only ever met with a welcoming learning environment from the Musser lab. I would also like to express specific thanks to my mentor Scott Renken, who I credit to being one of the greatest teachers I've ever had. Lastly, I thank the CCMR REU faculty and the 2021 cohort for making this summer such a great experience.

This work was supported by the Cornell Center for Materials Research with funding from the NSF Research Experience for Undergraduates program (DMR-1757420 and DMR-1719875).

## References

1. Lidzey, David & Coles, David. (2015). "Strong Coupling in Organic and Hybrid-Semiconductor Microcavity Structures." 243-273. 10.1007/978-3-319-16580-6\_11.
2. H. Ibach & H. Lüth (2009). "Solid State Physics." 4th edition. Springer Verlag

# Application of Basis Splines for Training a Semi-Empirical and Constraint Satisfying Density Functional Approximation

Trine K. Quady,<sup>1,2, a)</sup> Zachary M. Sparrow,<sup>2</sup> Brian G. Ernst,<sup>2</sup> and Robert A. DiStasio Jr.<sup>2</sup>

<sup>1)</sup>*Department of Chemistry, Portland State University, Portland, OR 97205 USA*

<sup>2)</sup>*Department of Chemistry and Chemical Biology, Cornell University, Ithaca, NY 14853 USA*

(Dated: 24 August 2021)

The performance of Kohn-Sham density-functional theory is governed by the accuracy of a density functional approximation (DFA) to approximate the exchange-correlation energy. Historically, DFAs are constructed using either non-empirical techniques that satisfy known quantum mechanical constraints, or semi-empirical techniques that fit the functional to benchmark data. In this work a method to construct DFAs that are both constraint satisfying and data driven is presented. This method is developed by applying cubic basis splines (B-Splines) optimized with penalization splines (P-Splines) to construct the inhomogeneity correction factor. A proof of concept of this method is demonstrated by the resulting global hybrid generalized gradient approximation, CASE21. CASE21 satisfies all but one of the constraints satisfied by the popular PBE0 functional while also being data-driven. This constraint satisfying semi-empirical functional is shown to outperform PBE0 on many chemical properties.

## INTRODUCTION

Theoretical chemistry investigates chemical structure and dynamics using the tools of quantum mechanics, statistical mechanics, and computation. A central aim for theoretical chemistry is to predict results and provide explanations for experiment. This quest is contributed to by three main pillars of theory: theory development, algorithms and implementation, and application. All of these aspects work in conjunction to develop a robust theoretical framework for investigating modern chemistry. This work is focused on method development, which seeks to build and improve upon foundational tools within theoretical chemistry.

Kohn-Sham density-functional theory<sup>1,2</sup> (KS-DFT) is the most popular method for modelling systems quantum mechanically. Within the various computational approaches to the study of electrons in matter, KS-DFT balances performance and accuracy making it the computational workhorse in physics, materials science, and chemistry communities. The total ground-state energy in KS-DFT may be calculated by

$$E_{KS}^{DFT} = T_s[\{\phi\}] + E_{NN} + E_{eN}[\rho] + J[\rho] + E_{xc}[\rho] \quad (1)$$

where  $T_s[\{\phi\}]$  is the mean-field kinetic energy,  $E_{NN}$  is the nuclear-nuclear potential energy,  $E_{eN}$  is the electron-nuclear potential energy,  $J[\rho]$  is the Coulombic repulsion potential energy, and  $E_{xc}$  is the exchange-correlation energy which contains the non-trivial kinetic and non-classical electron-electron interaction energies which bridge the gap between the Hartree approximation and the exact solution to the energy. As the first four

terms in Eq. (1) are known exactly, all approximation in KS-DFT lies within the  $E_{xc}$  term.

Density functional approximations (DFA) are developed to approximate the  $E_{xc}$ . Chemists and physicists alike have developed many DFAs, or more generally functionals, to provide quantitative information concerning various many-bodied systems. A common goal in DFA development is to increase the accuracy of the functional while decreasing the computational cost. Unique to KS-DFT, the addition of more quantum mechanical information to a DFA does not guarantee improved accuracy from the functional. However, in 2001 Perdew constructed a now infamous "Jacob's ladder" of KS-DFT approximations which outlines a hierarchy of exchange-correlation DFAs where each successive rung contains more sophisticated information concerning the electron density<sup>3</sup>. The bottom of the ladder rests in the Hartree realm where there is no contribution from exchange-correlation energy in the functional ( $E_{xc} = 0$ ). The first rung of five is the local spin density approximation (LSDA), the simplest of the exchange-correlation functionals as it only makes use of the electron density ( $\rho$ ). The LSDA may be exact for the infinite uniform electron gas (UEG) limit, however, this approximation is inaccurate in systems of inhomogeneous electron density such as systems involving atoms and molecules. The second rung is the generalized gradient approximation (GGA), which incorporates the density gradient ( $\nabla\rho$ ) to better account for the effects of inhomogeneity in the electron density on  $E_{xc}$ . Notable GGA functionals include Perdew's PBE<sup>4</sup> and Becke's BLYP<sup>5,6</sup>. The third rung is the meta-GGA which includes the Laplacian of the electron-density ( $\nabla^2\rho$ ) or the kinetic energy density leading to functionals such as TPSS<sup>7</sup> and SCAN<sup>8</sup>. The fourth rung is the global hybrid GGA which incorporates exact-exchange ( $E_{xx}$ ) into the GGA type functional to partially account for self-interaction

<sup>a)</sup>Electronic mail: tkq2@cornell.edu

error, a functional's inability to distinguish between interactions between two particles or interaction of a particle with itself. This mixing of  $E_{xx}$  and  $E_{xc}$  has produced some of the most popular functionals such as PBE0<sup>9</sup>, B3LYP<sup>10</sup>, and B97<sup>11</sup>. The fifth and last identified rung below the "heavens" of chemical accuracy is the double hybrid, which use information from the wave-functions, including the unoccupied orbitals, for the exchange and correlation expressions. With each successive rung the sophistication of the functional increases, however, with increased sophistication involves increased computational cost. Therefore, in order to effectively implement a DFA one must weigh complexity and computation to fit the needs of the application.

There have been many approaches to develop DFAs, most broadly the two categories of DFAs fall within non-empirical and semi-empirical strategies. Non-empirical DFAs are designed to ensure the functional satisfies known quantum mechanical constraints. This approach lends itself to greater transferability among systems, a desirable trait in physics communities. Notable non-empirical functionals include PBE, TPSS, and SCAN. In contrast, semi-empirical DFAs are designed by fitting a DFA to benchmark data, generally using a power series expression for the inhomogeneity correction factor (ICF) whereby the coefficients are determined almost exclusively by the reference data. This data-driven approach tends to have greater accuracy than a non-empirical functional on chemical systems similar to those used to train the functional. This focused accuracy is desirable in chemistry communities. A potential concern for semi-empirical methods is over-fitting. Ridge-regression is often implemented to avoid this by penalizing the magnitude of the coefficients used to fit the functional. The semi-empirical approach is responsible for functionals such as B3LYP, B97, and  $\omega$ B97X-V<sup>12</sup>.

In this work we aim to unite transferability and accuracy by creating a method that combines constraint satisfying and data driven characteristics into a single functional. A proof-of-concept of this method is presented in the global hybrid GGA CASE21 – **C**onstrained **A**nd **S**moothed semi-**E**mpirical **2021**. CASE21 approximates the  $E_{xc}$  by separating the exchange and correlation contributions and incorporating 25%  $E_{xx}$ .

$$E_{xc}^{\text{CASE21}} = \frac{3}{4}E_x^{\text{CASE21}} + \frac{1}{4}E_{xx} + E_c^{\text{CASE21}} \quad (2)$$

The  $E_x^{\text{CASE21}}$  and  $E_c^{\text{CASE21}}$  terms are similarly expressed in a multiplicative form as

$$E_a^{\text{CASE21}}[\rho] = \int \rho \epsilon_a^{\text{LDA}}(\rho) F_a(u_a) d\mathbf{r} \quad (3)$$

where  $a = x$  or  $c$  to represent the exchange and correlation components, respectively.  $\rho$  is the electron density,  $\epsilon_a^{\text{LDA}}$  is the exchange energy density per particle of the local density approximation (LDA) when  $a = x$  and

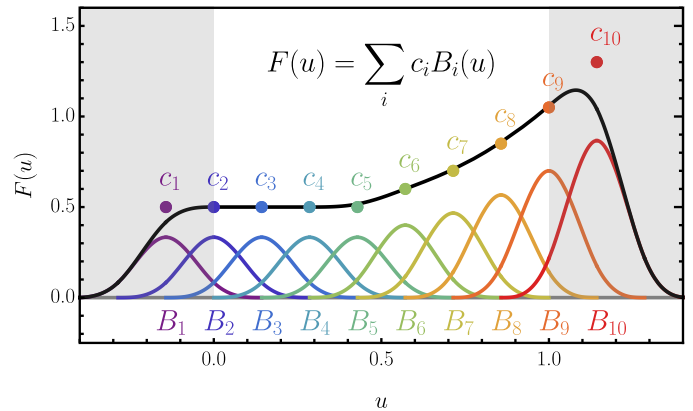


FIG. 1. B-spline basis functions (rainbow) that construct the CASE21 ICFs. A linear combination of each B-Spline ( $B_i$ ) scaled by a coefficients ( $c_i$ ), represented by the equation for  $F(u)$ , forms the resulting smooth function (black).  $c_i = 1/2$  for  $i \leq 5$  representing a linear function of B-Splines,  $c_i$  for  $i \geq 6$  represents a flexible function of the B-Splines.

the correlation energy density per particle of the PW92 LDA correlation functional<sup>13</sup> when  $a = c$ . Lastly,  $F_a(u_a)$  is the ICF. The functional form of  $E_a$  can be made, within the training procedure, to satisfy all exchange constraints and all but one of the correlation constraints that are satisfied by the PBE0 functional. However, in principle this method may be used to satisfy all of the PBE0 correlation constraints by adopting the  $E_c^{\text{PBE0}}$  functional form.

The method presented in this work utilizes basis splines (B-Splines)<sup>14</sup> to form the basis functions of the exchange and correlation ICFs. These piece-wise cubic uniform B-splines provide local support under each spline which is scaled by a coefficient ( $c_i$ ) as seen in FIG. 1. A linear combination these splines form a function that is highly flexible and continuous up until the  $n - 2$  derivative where  $n$  is the order of the splines (in this case  $n = 3$ ). The  $c_i$  of each spline make up the 'backbone' of the resulting function, therefore by fitting these  $c_i$  to benchmark data we may construct an ICF that is data-driven. Application of these B-Splines in the functional form given in Eq. (3) allows both satisfaction of constraints while being semi-empirical.

In order to optimize CASE21 and avoid overfitting after training the functional we implement penalization splines (P-Splines)<sup>15</sup>. P-Splines penalize "wiggleness" in the ICF ensuring smoothness by applying a finite difference penalty on the B-Splines  $c_i$ . This method determines  $\{c_i\}$  by minimizing the loss function represented by

$$\begin{aligned} \text{Loss} = & \text{goodness of fit} + \\ & \lambda \times \text{smoothness term} \\ & + \text{constraints term} \end{aligned} \quad (4)$$



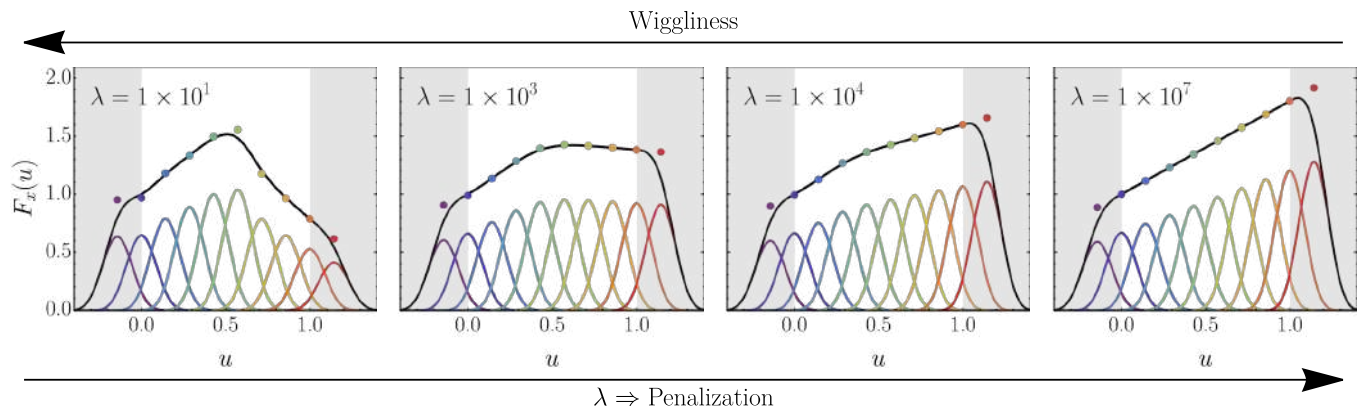


FIG. 2. The impact of  $\lambda$  on the CASE21 exchange ICF, whereby the level of penalization (magnitude of  $\lambda$ ) is inversely proportional to the wigginess in the functional. This demonstrates the enforcement of smoothness as a constraint in CASE21.

where  $\lambda$  is the hyperparameter responsible for the degree of smoothing that takes place by these P-Splines on the fit ICF. An example of this relationship may be seen in FIG. 2 where the magnitude of  $\lambda$  controls the degree of penalization and therefore smoothness on the ICF. As  $\lambda \rightarrow \infty$  the ICF tends toward linearity. We may optimize this balance between flexibility and smoothness to assign a  $\lambda$  value that maintains smoothness in the ICF while still allowing data driven influence.

The flexibility of applying B-Splines as a basis function not only allows the functional to be semi-empirical but also allows the satisfaction of constraints. To demonstrate this constraint satisfaction the exchange and correlation ICFs may be represented as linear functions.

$$F_x(u_x) = 1 + 0.804 \times u_x \quad (5)$$

$$F_c(u_c) = 1 - u_c \quad (6)$$

The finite-domain variable  $u_a$  is constructed such that these parameter-free expressions for  $F_a(u_a)$  maintain satisfaction of all intended constraints and therefore may be used to visualize these constraints in FIG. 3. The piece-wise nature of the splines allow the enforcement of all explicit constraints (*e.g.* UEG limit and rapidly varying density limit) to only depend on the B-splines in the  $u$  domain where the constraints are being enforced. Therefore the constraints may be treated as priors to be satisfied while all of the unconstrained splines may remain flexible to be fit to data. All of the implicit constraints on the functional (*e.g.* Lieb-Oxford Bound and negativity of the exchange energy) may be implemented with a generalized form of Tikhonov regression. In this way the CASE21 functional satisfies all of the following constraints: exact exchange spin scaling, uniform density scaling for exchange, UEG limit for exchange and correlation, UEG linear response, Lieb-Oxford bound, negativity of the exchange energy, second order gradient response for correlation, rapidly varying density limit for correlation, non-positivity of the correlation energy,

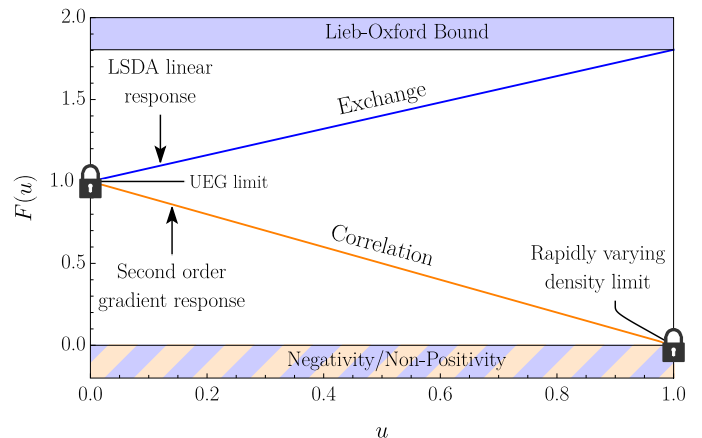


FIG. 3. Linear representations of the exchange (blue) and correlation (orange) ICFs and the implicit and explicit constraints they satisfy within the  $u$  domain.

and lastly ICF smoothness. However, the representation of  $E_c^{\text{CASE21}}$  in Eq. (3) does not allow the enforcement of proper uniform scaling to the high-density limit in the correlation that PBE0 does satisfy.

The functional training procedure uses three sets of benchmark data: the training, validation, and testing set. The training set is used to create many  $\{c_i\}$  each corresponding to an individual  $\lambda$ . The validation set is used to determine which  $\lambda$  minimizes the weighted root-mean-squared error (wRMSE) on this set. This optimized  $\lambda$  is used to refit the functional on the training and validation sets. The testing data is then used to evaluate the fit functional. The CASE21 training and validation sets contain a small number of chemical properties whereas the testing set contains a diverse range of data, therefore achieving good performance on the testing set shows transferability of the functional. The CASE21 training set contains heavy atom transfer energies (HAT), the validation set contains total at-

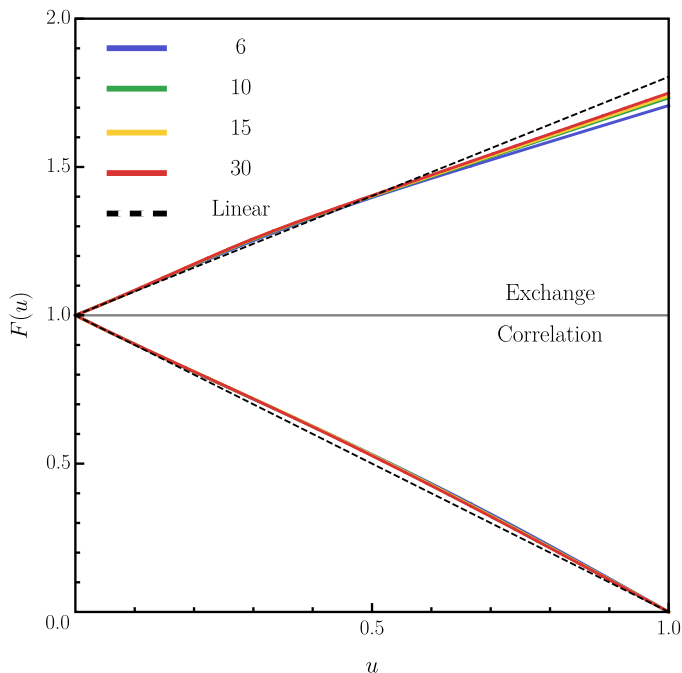


FIG. 4. CASE21 exchange and correlation ICFs for 6 (blue), 10 (green), 15 (yellow), and 30 (red) B-spline cases with linear unfit ICFs (black dashed). Any deviation of the ICFs from linearity is purely data driven.

omization energies (TAE), and absolute energies (AE). The testing set contains reaction energies (RXN), bond dissociation energies (BDE), proton affinities (PA), reaction barrier heights (BH), ionization potentials (IP), electron affinities (EA), isomerization energies (IE), and non-covalent interaction energies (NCI).

This training procedure was used to fit the CASE21 ICFs, using a  $\frac{\partial^2 f}{\partial x^2}$  penalization for  $\lambda$ , on 6, 10, 15, and 30 splines. These ICFs are depicted in FIG. 4 along with the linear ICFs (black dashed) from Eqs. (5) and (6). Since the parameter free ICFs may be plotted as linear functions, any deviation from linearity in the CASE21 ICFs indicate a direct data-driven influence that a purely constraint-satisfying functional would not have. The resulting flexibility in these optimized ICFs cannot be obtained with a low order polynomial as the basis support of each spline provides a more domain independent approach to creating a functional. Plotting the ICFs with differing numbers of splines shows there is little dependence of the ICF on the number of splines with slight deviation in the  $u \rightarrow 1$  region of the exchange ICF. The correlation ICF on the other hand maintains a more uniform consistency between the spline cases. The 10 spline case was chosen as the final CASE21 functional as it maintains flexibility while not risking overfitting with too many splines. The 10 spline ICF also falls within the middle of the ICFs being bounded above and below by the 30 and 6 spline cases, respectively in the

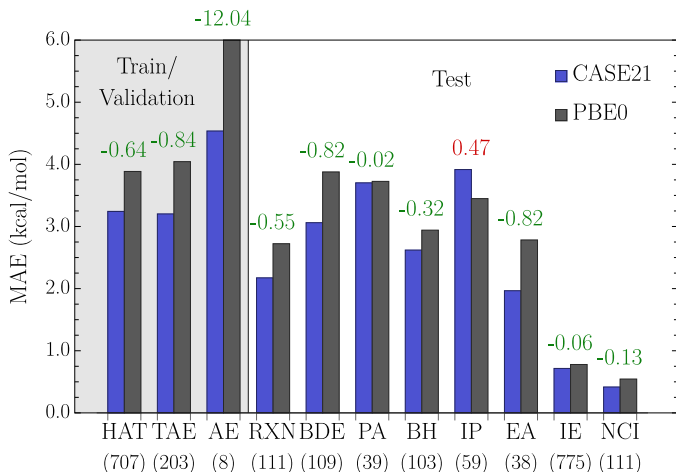


FIG. 5. MAE in kcal/mol of the CASE21 functional compared to PBE0 by chemical property, with the number of data points in each property indicated below each property label. Negative labels (green) indicate how much CASE21 improves upon the PBE0 error and positive labels (red) indicates how much greater the MAE of CASE21 is than PBE0. The data contains: HAT – heavy atom transfer energies, TAE – total atomization energies, AE – absolute energies, RXN – reaction energies, BDE – bond dissociation energies, PA – proton affinities, BH – reaction barrier heights, IP – ionization potentials, EA – electron affinities, IE – isomerization energies, and NCI – non-covalent interaction energies.

exchange. CASE21 contains 1.27 degrees of freedom, a further testament to ensuring the 10 spline case is not overfit.

The CASE21 functional was compared with PBE0 to evaluate the accuracy of the DFA against a widely used constraint satisfying functional. The results of this error analysis may be seen in FIG. 5 where the mean absolute errors (MAE) of CASE21 and PBE0 are compared and grouped by various chemical properties. Given that CASE21 was trained and validated on heavy atom transfer energies, total atomization energies, and absolute energies we see measurable improvement from the PBE0 functional, as expected. The most meaningful evaluation lies within comparing the functionals to diverse unknown data in the testing set. Within this set CASE21 outperforms PBE0 on seven out of the eight chemical properties with the most substantial improvements on reaction energies, bond dissociation energies, and electron affinities. CASE21 has a greater MAE than PBE0 on ionization potentials, while the two functionals are comparable on proton affinities. This over-all general improvement of CASE21 on the testing data, despite being trained on a very few types of chemical properties demonstrates that uniting constraint satisfaction with a semi-empirical functional form may produce a more transferable and accurate functional. This method to unite constraints and data provides a tool that may be used to improve upon, and build future DFAs.

## CONCLUSIONS

Within this work we presented a method that utilizes B-Splines, optimized with P-Splines, to train a constraint satisfying and data driven DFA. As a proof-of-concept for this method the semi-empirical global hybrid GGA CASE21 was constructed, satisfying 11 quantum mechanical constraints. This functional demonstrated both transferability and accuracy by out-performing the purely constraint satisfying PBE0 functional on a diverse set of chemical properties. Future work consists of self-consistently optimizing CASE21 and applying this method of B-Splines to a double-hybrid GGA.

## ACKNOWLEDGEMENTS

I would like to express my deepest gratitude to Dr. Robert A. DiStasio Jr. for the opportunity to work in his lab group and Laura E. Rutherford for helping make this experience possible. I would also like to thank my mentors Zachary M. Sparrow and Brian G. Ernst for their help and leadership in teaching me about research in the the fields of theoretical and computational chemistry. Lastly, I would like to thank the Cornell Center for Materials Research Research Experience for Undergraduates (CCMR REU) program for providing this research experience at Cornell University.

## FUNDING

This project was supported in part by the CCMR with funding from the REU program via the National Science Foundation under the award number DMR-1757420 and DMR-1719875.

## REFERENCES

- <sup>1</sup>P. Hohenberg and W. Kohn, "Inhomogeneous Electron Gas," *Phys. Rev.* **136**, B864–B871 (1964).
- <sup>2</sup>W. Kohn and L. J. Sham, "Self-Consistent Equations Including Exchange and Correlation Effects," *Phys. Rev.* **140**, A1133–A1138 (1965).
- <sup>3</sup>J. P. Perdew and K. Schmidt, "Jacob's ladder of density functional approximations for the exchange-correlation energy," *AIP Conference Proceedings* **577**, 1–20 (2001).
- <sup>4</sup>J. P. Perdew, K. Burke, and M. Ernzerhof, "Generalized Gradient Approximation Made Simple," *Phys. Rev. Lett.* **77**, 3865–3868 (1996).
- <sup>5</sup>A. D. Becke, "Density-functional exchange-energy approximation with correct asymptotic behavior," *Phys. Rev. A* **38**, 3098–3100 (1988).
- <sup>6</sup>C. Lee, W. Yang, and R. G. Parr, "Development of the Colle-Salvetti correlation-energy formula into a functional of the electron density," *Phys. Rev. B* **37**, 785–789 (1988).
- <sup>7</sup>J. Tao, J. P. Perdew, V. N. Staroverov, and G. E. Scuseria, "Climbing the Density Functional Ladder: Nonempirical Meta-Generalized Gradient Approximation Designed for Molecules and Solids," *Phys. Rev. Lett.* **91**, 146401 (2003).
- <sup>8</sup>J. Sun, A. Ruzsinszky, and J. P. Perdew, "Strongly Constrained and Appropriately Normed Semilocal Density Functional," *Phys Rev Lett* **115**, 036402 (2015).
- <sup>9</sup>C. Adamo and V. Barone, "Toward reliable density functional methods without adjustable parameters: The PBE0 model," *J. Chem. Phys.* **110**, 6158–6170 (1999).
- <sup>10</sup>A. D. Becke, "Density-functional thermochemistry. III. The role of exact exchange," *J. Chem. Phys.* **98**, 5648–5652 (1993).
- <sup>11</sup>A. D. Becke, "Density-functional thermochemistry. V. Systematic optimization of exchange-correlation functionals," *J. Chem. Phys.* **107**, 8554–8560 (1997).
- <sup>12</sup>N. Mardirossian and M. Head-Gordon, " $\omega$ B97X-V: A 10-parameter, range-separated hybrid, generalized gradient approximation density functional with nonlocal correlation, designed by a survival-of-the-fittest strategy," *Physical Chemistry Chemical Physics* **16**, 9904–9924 (2014).
- <sup>13</sup>J. P. Perdew and Y. Wang, "Accurate and simple analytic representation of the electron-gas correlation energy," *Phys. Rev. B* **45**, 13244–13249 (1992).
- <sup>14</sup>C. DE Boor, "B(asic)-Spline Basics." Tech. Rep. (Wisconsin University-Madison Mathematics Research Center, 1986).
- <sup>15</sup>P. H. C. Eilers and B. D. Marx, "Flexible smoothing with B-splines and penalties," *Statistical Science* **11**, 89–121 (1996).

# Biologically surprising preliminary result from novel pulse height analysis of an optical cell proliferation apparatus

Ron Volkovinsky<sup>1</sup>, Carl Franck<sup>2</sup>

<sup>1</sup> Department of Chemical Engineering, Georgia Institute of Technology, Atlanta, GA 30332, USA

<sup>2</sup> Laboratory of Atomic and Solid State Physics, Cornell University, Ithaca, NY 14853, USA

## Abstract

Typical methods of analyzing cellular proliferation such as hemocytometer assays disturb cell clusters and yield poor temporal resolution. Therefore, our group developed a novel optical cell proliferation counting apparatus to more accurately observe the social amoeba *Dictyostelium discoideum*. This paper describes a computational technique to analyze pulse data generated from the counting apparatus. Efficacy of the technique is shown by analyzing colloidal samples and comparing their pulse height distributions to those of live samples. Finally, modeling attempts of *D. discoideum* proliferation dynamics are furthered by providing evidence counter to the current prevailing hypotheses of clustering behavior.

## Introduction

The transition from unicellular to multicellular life is a key step in the history of evolution, occurring independently in the development of algae, plants, animals, and fungi (6). Once formed, multicellular organisms experience increased fitness due to cellular differentiation and the resulting functional specialization (4, 14). This adaptation is apparent in the starvation state of the cellular slime mold *Dictyostelium discoideum*. When starved, *D. discoideum* aggregates into a multicellular organism with differentiated cells (5). This complex behavior has merited intense study into the many mechanisms behind *D. discoideum*, with the organism eventually becoming a common NIH model (11). Therefore, the organism was a natural starting point to explore the origins of multicellular life.

A commonly proposed evolutionary mechanism for the development of multicellular organisms starts with the formation of simple undifferentiated cell clusters (9, 10). It is widely known that *D. discoideum* exhibits multicellular behavior in the starvation state. Less commonly studied however is the behavior that occurs during the organism's vegetative state, namely the lagging and exponential phases. The lag phase occurs in many cellular organisms and is characterized by a period of slower growth before typical exponential growth (2, 8). Despite over a century of observation, the biological processes and spatiotemporal dynamics that occur during the lag phase and subsequent transition into log phase are poorly understood (12). Biologists have long assumed that the lag phase allows for cells to acclimate to changes in culturing environment such as available food, temperature, cell density, and surrounding microorganisms (11).

When a lag-log transition is purely mediated by density, the organism is said to be subject to an Allee effect (1). In a word, the Allee effect is characterized by the presence of 'undercrowding', or the ability of low cell density alone to decrease cellular growth rate (13). Although laboratory guidelines have mentioned the effect of density on *D. discoideum* growth



rate (5), only recently has rigorous experiment been undertaken to demonstrate the presence of an Allee effect (7). A further observation in the proliferation dynamics of *D. discoideum* is a high degree of variability in the lagging phase. It typically lasts around 29 hours, but may range in length from -20 to +120 hours (7).

The Allee effect may arise from various cell communication or signaling mechanisms. Juxtacrine mechanisms are contact-mediated, the cells sense each other's presence through physical contact. Endocrine mechanisms are governed by growth factors that are produced by the cells and then uniformly distributed throughout the medium. Previous works have provided evidence against the juxtacrine mechanism by observing no change in lag phase even when the degree of cell-cell contact was altered (7). The works' formulation of the endocrine mechanism also did not approach a similar degree of variation in the lag phase compared to what is observed in experiment (7). The next models to be tested were cluster-based theories. Cluster-based endocrine signaling posits that growth factor is produced by cellular clusters and affects cells throughout the whole sample. In paracrine signaling, growth factor is only produced within clusters, and affects only cells within that cluster. These cluster-based models are far from perfect, but offer a reasonable and falsifiable hypothesis to examine.

To experimentally investigate the clustering hypotheses, we used a novel optical cell passage counter (OCPC) assay (7). This assay provided the capability to study cell populations *in vitro*, with high temporal resolution, and at a wide range of cell densities. The advantages of studying cell populations *in vitro* are clear. When counting cells with a typical hemocytometer assay, the cells are transferred to a counting chamber with a pipette, introducing shear forces which are likely to destroy clusters. The capability to study cell populations over indefinite time periods and a range of cell densities allowed the capturing of highly precise proliferation dynamics. The OCPC assay has proven to be a powerful tool to study cell populations, but the data it generates can be difficult to analyze. A data pipeline was developed in MATLAB that allows for better data analysis and visualization than ever before. Through this new technique, we have gained biological insight that will push forward research into the cellular dynamics that occur during the proliferation of *D. discoideum* colonies.

## Methods

### *Automated Continuous Counting Method*

The OCPC setup was developed to obtain measurements of cell density in an automated, continuous fashion over long time periods (Figure 3) (7). The setup involves a red laser diode source focused onto the center of a test chamber by a low-power objective lens. The chamber is a 0.75-inch diameter cut test tube capped with a rubber septum, and can hold 10 mL of liquid. A magnetic stir bar at the bottom of the cell is driven by a permanent magnet rotated by a stepper motor. A relay lens images the laser-illuminated region of the sample onto a fast, single-pixel light detector. All components are covered in a light-shielding box to minimize noise.

The data obtained from the counter is in the form of voltages outputted from the light detector. These voltages are passed through a pre-amp, low-pass filter, and then a variable gain stage before entering a computer. The computer parses them through the Audacity audio program, where they are then exported as .flac files. Each pulse in the file is a detection event.

With this setup, we can capture a range of cell counts from densities of  $10^2$  cells/mL up to  $10^5$  cells/mL. This range is capped by a pileup which occurs when the detector fails to discretize individual light pulses due to high cell density. However, the range still easily captures the lag-log transition phase and allows us to measure it with high accuracy.

We use MATLAB to analyze and reduce the data obtained from the assay. Our data is in the form of .flac audio files, which can be processed by the *audioread* function, which returns an audio data array and an integer representing the sampling rate. Each column in the audio data array is representative of an audio channel; in our case, the first audio channel contains all of our data. The unmodified behavior of *audioread* for .flac files results in data represented as type `uint8`. Therefore, the data will be normalized to be between 0 and 255. Once the audio data array is in the workspace, the function *findpeaks* can be used to find local maxima within the data. The use of this function was suggested by Zijin Huang. The function returns the location and height of each maximum point that it finds as a vector. The behavior of the function can be modified with name-value pairs. We wanted to select for peaks that were generated by objects passing through the laser volume, and not background noise. However, we didn't want to use a simple peak height requirement, because we wanted to track even small objects which generate small peaks. Therefore, we decided to use and tune *MinimumPeakProminence* modifier. This modifier measures the prominence of a peak, which is a measure of how much a peak stands out from nearby peaks. Prominence is determined from both intrinsic peak height and location relative to neighboring peaks. By setting the correct prominence threshold, we will still measure isolated low peaks, but not the constant stochasticity throughout the audio file.

A further challenge in the analysis of our audio files was their size. When attempting to use the audio reading function provided by MATLAB on our multi-hundred-hour audio files, a typical computer would run into memory bounds. To circumvent this, a variety of techniques from MATLAB's big data toolbox were employed. The novel program reads and analyzes 30 minute sections of the audio file, and saves each analysis as a MATLAB file, removing it from working memory. From there, the files are all collected into a *FileDataStore* using a custom file reading function. From there, the program creates a 'tall' array on top of the datastore. Tall arrays are used to work with out-of-memory data and can be arbitrarily large in the first dimension. They allow common functions such as *mean*, *std*, and *histogram* to be used on massive data sets, and are the method employed to greatly simplify data analysis.

### *Cell Culture*

Cell culturing followed standard shaker culture protocols (5). Agar plates inoculated with AX4, a common axenic strain of *Dictyostelium discoideum* was received from Northwestern University Dicty Stock Center. The cells were plated into 2 mL of HL5 culture media in a 25 mm diameter Falcon dish. The dishes were then sealed with parafilm. From there, cells were monitored and allowed to proliferate to a density of about  $1E04$  cells per milliliter. The cells were then transferred to 50 mL Falcon tubes with an additional 3 mL of HL5 culture media. The Falcon tubes were placed on an orbital shaker. Cells are continuously monitored and split into new 50 mL Falcon tubes when reaching a density of about  $1E07$  cells per milliliter.

### *Manual Cell Counting*

When manually counting cells, standard Nageotte and Neubauer hemocytometer counting techniques were used (8). Pipettes and counting chambers were sterilized with a 65% by volume

mixture of isopropyl alcohol with water. Before pipetting, Falcon tubes were agitated to suspend cells from the bottom of the culture media.

### *Colloidal sample preparation*

Colloidal samples were measured by the OCPC assay to obtain the frequency response of the system with a standard set of particles. To prepare a colloidal sample, 10-micron Polybead polystyrene microspheres (Cat#17136) was vortexed and sonicated until well mixed. Then, one drop was added to 10 mL distilled water in a 15 mL Falcon tube. The colloid density was measured with a hemocytometer. The sample was then diluted to 1E04 colloids/mL in 50 mL falcon tubes full of distilled water. These were the mixtures measured by the OCPC assay.

## **Results**

The MATLAB code was run on a sample which was inoculated at 100 cells/mL and allowed to run in the OCPC apparatus for 115 hours. This data was collected by Zijin Huang, Christopher Donohue, Reiley Dorian, and Carl Franck. The code generated Figures 1 and 2, allowing for new statistical analyses to be made from previously collected data. Figures 1a, b, and c show pulse height histograms at varying points during the cell growth cycle. There is a clear trend of decreasing mean and standard deviation of pulse heights over time. Figure 1d, the colloidal sample, shows a pulse height histogram of 10-micron polystyrene colloidal particles in suspension. Notably, the standard deviation of pulses in Figure 1d is lower than the standard deviation of any other point in the analysis. The analyses of live cells show a clear skew to the right end of the distribution, with skew values consistently greater than 1. This trend is not seen as clearly in the relatively symmetrical colloidal sample, which has a skew value much closer to 1. Figure 2 shows cell density over an entire run. Each point in figure 2 represents the number of pulses in the last 300 seconds, with the color representing the average pulse height over that time in arbitrary units. There is a very pronounced initial sudden rise in cell density, a long lag phase, and a clear exponential phase.

## **Discussion**

Efficacy of the OCPC assay was shown with an analysis of colloidal mixtures. The standard deviation of pulse heights observed in the colloidal mixture was a factor of 3 lower than the next lowest standard deviation in the cellular samples. This is indicative of a relationship between particle size and pulse height. The pulse height distribution resulting from the colloidal sample is highly uniform because colloids are uniform in size. We would expect cells to be less uniform in size (either due to variations in single cells or clustering), so they should have a larger standard deviation, which is exactly what is observed. This difference in standard deviations between colloidal and live samples is therefore a promising verification of the OCPC assay's ability to relate particle size with pulse height.

The skew of the live samples is indicative of a distribution leaning towards larger peak heights than average. If higher peaks are truly indicative of larger particles, then larger than average objects are being detected by the laser in live samples. This is the opposite of the skew behavior in the colloidal sample, which is nearly symmetrical, indicative of a uniform distribution in both directions from the mean particle size.

The most perplexing results of our new data analysis method lie in the mean pulse heights over time of the sample. Promising mathematical models of *D. discoideum* proliferation

dynamics have focused on cell clustering. The two best performing models include the cluster-sourced endocrine signaling mechanism, where a growth factor produced by cell clusters is evenly spread throughout the media, and the paracrine signaling mechanism, where cells within the same cluster exchange growth factors. Both models predict that the number of cells in clusters should increase over time. Therefore, the preliminary results presented in this paper are opposite to expectations derived from mathematical signaling models.

## Conclusion

The new MATLAB code is a powerful tool for pulse height analysis of data generated from the OCPC apparatus. The efficacy of the code was verified through the analysis of a colloidal sample, which showed a significantly lower standard deviation than the live samples. The smaller pulse height distribution around the mean for the colloidal sample as compared to the distribution around the mean for the live cells is indicative of a relationship between pulse height and particle size. The code can therefore be used to visualize particle density and size distributions over time. The new analysis provides evidence that particle size decreases over time, especially by the time the exponential phase is reached. This is a surprising preliminary result that casts doubt on the ability of presented clustering models to explain the behavior of *D. discoideum* throughout the lag-log transition.

## Figures

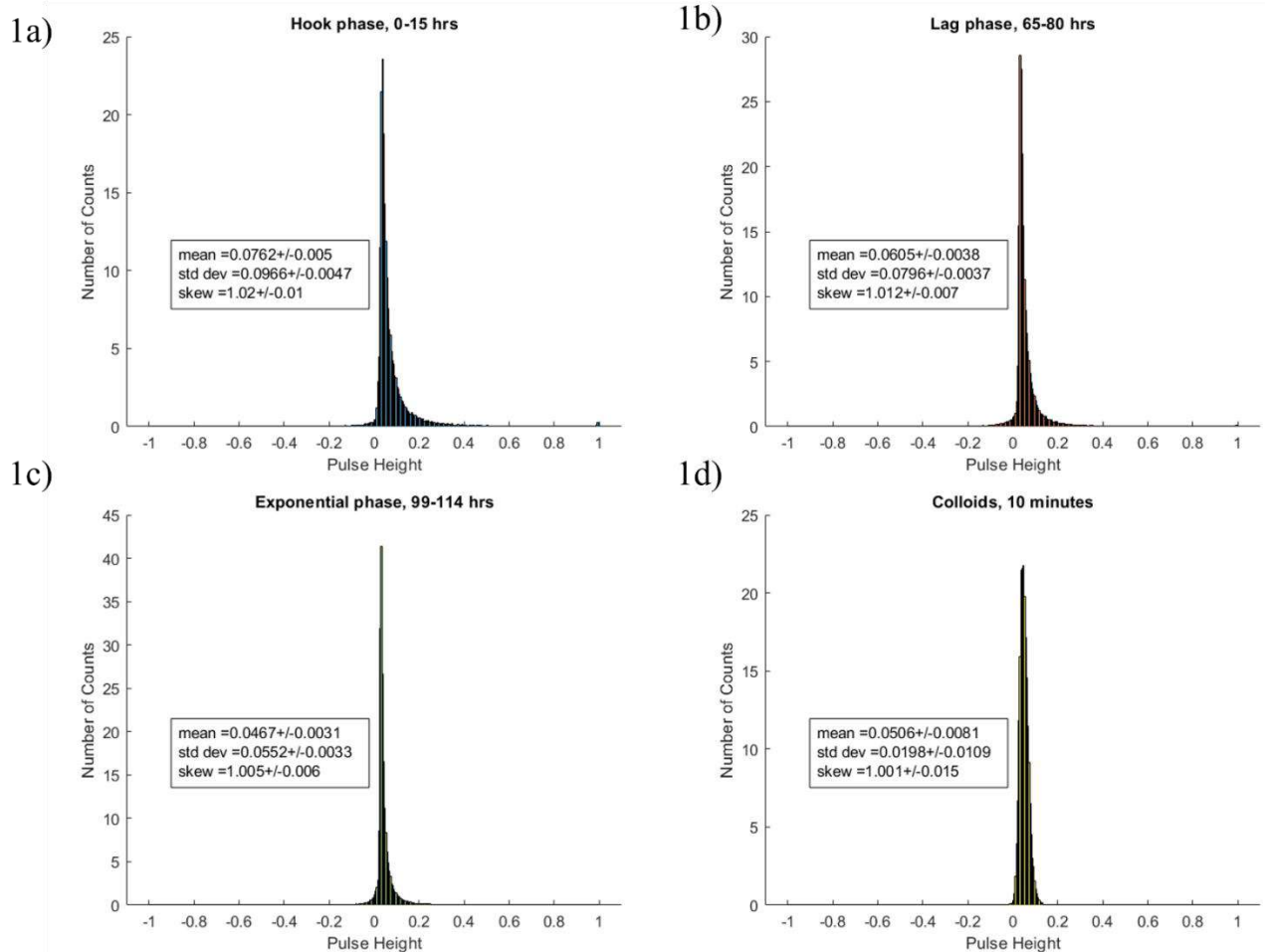




**Figure 1. Normalized pulse height frequency distributions.** These histograms were generated from the new MATLAB pipeline. They were normalized by taking the total number of observations in each bin and dividing that by the total number of observations multiplied by the width of the bin. The area of each bar is the relative number of observations, and the sum of the bar areas is equal to one. Each histogram represents the pulse height distribution and statistical information of data collected from the OCPC assay. a) Results for the first 15 hours of a sample cell starting at 100 cells/mL. b) Results for the middle 15 hours of the run started in figure 1a. c) Results for the last 15 hours of the run started in figure 1a. d) Results for a 10-minute run of a sample of 10-micron polystyrene colloids.

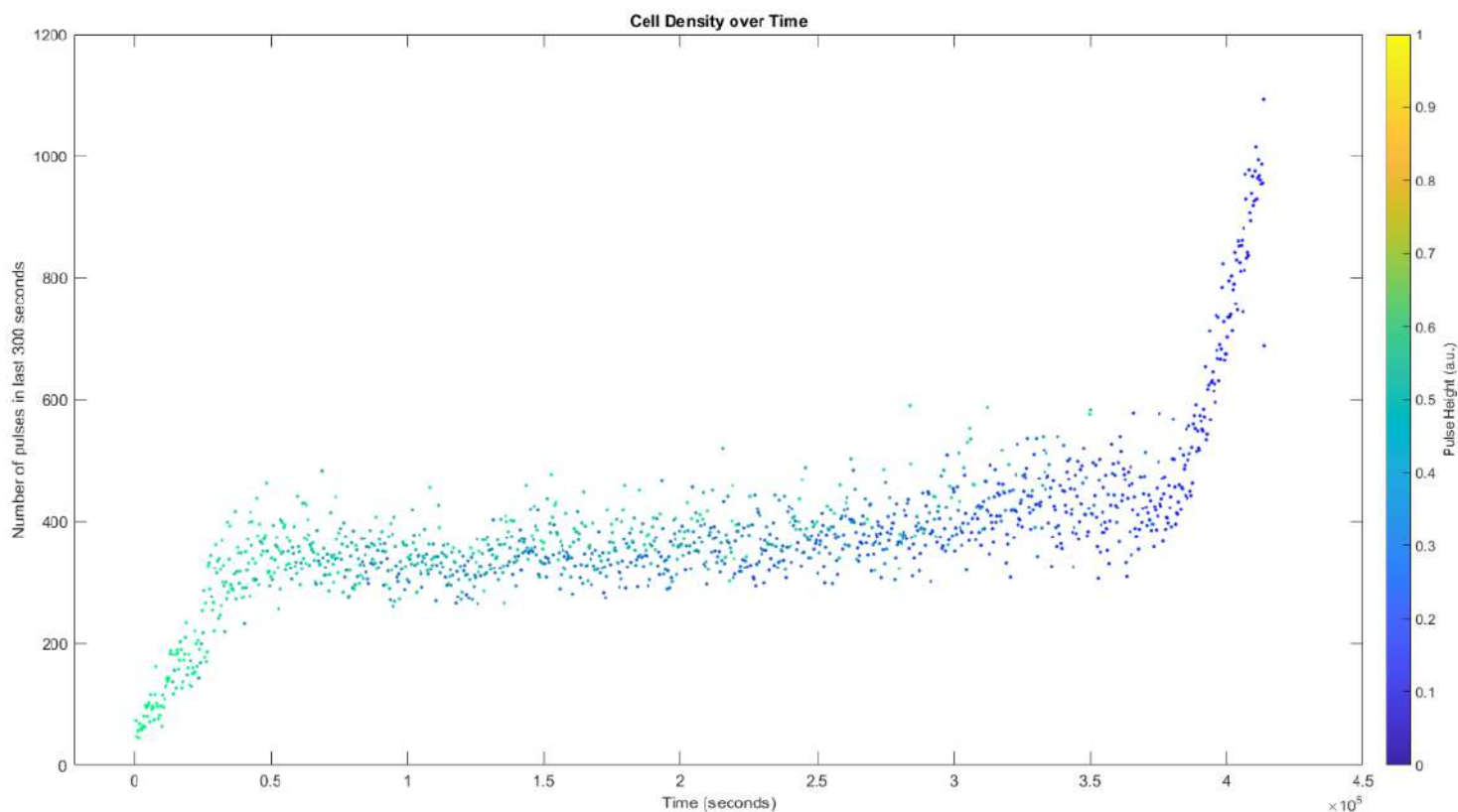


**Figure 2. Plot of cell culture over 115 hours starting from low cell density.** The plot was generated with new MATLAB method. Each point on the plot represents the number of pulses over the past 300 seconds before that point. The color of the point is indicative of the pulse height; where lighter blue is a higher average pulse height over the last 300 seconds, and darker blue is a lower average pulse height over that time.

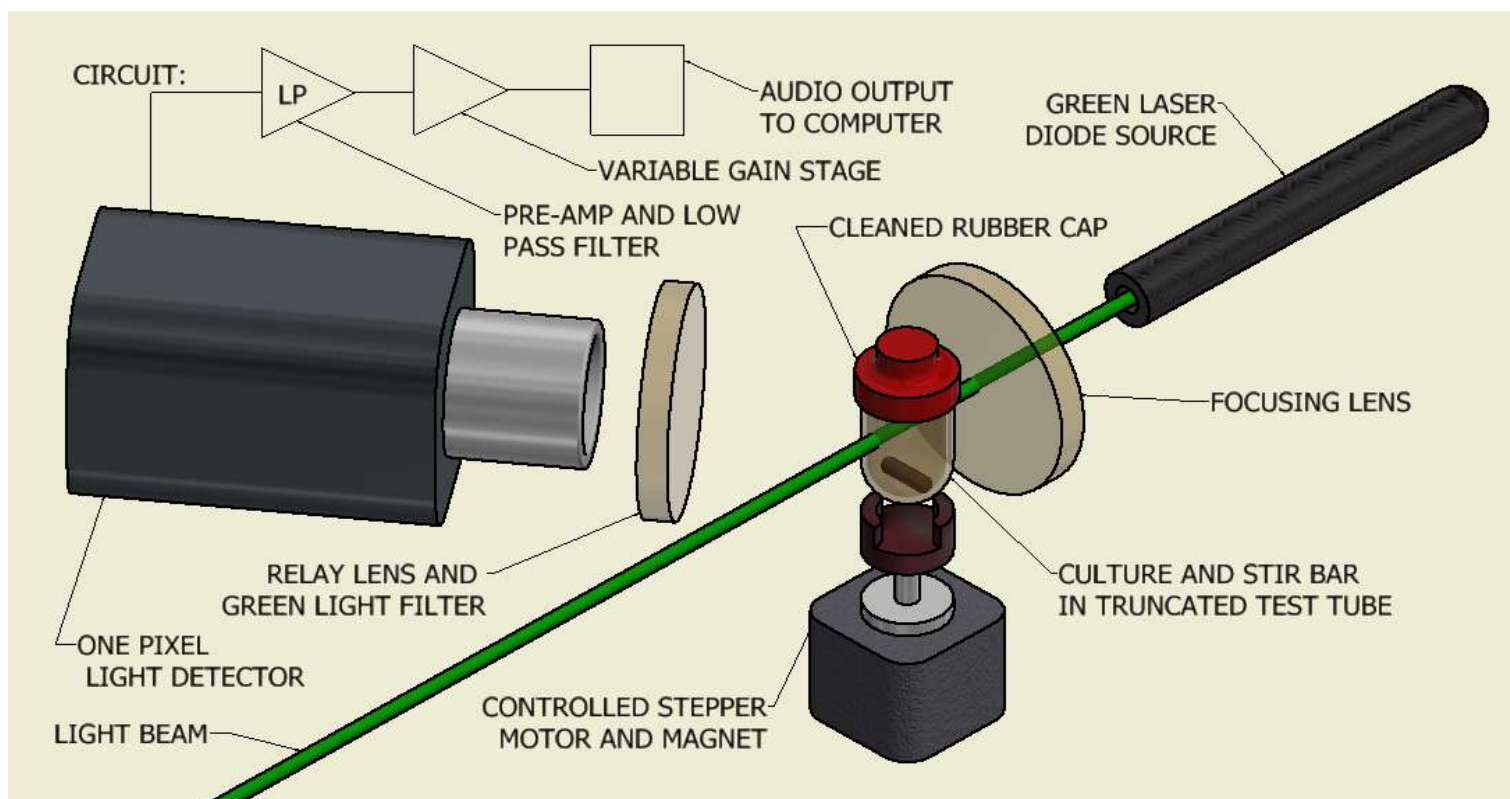


**Figure 3. Optical Cell Passage Counting Apparatus (From reference 7).** Schematic (not to scale) diagram showing important components and signal processing chain of our automated cell counting system for observing a stirred suspension culture.

## References

1. Allee WC. Animal aggregations, a study in general sociology. Chicago :: The University of Chicago Press; 1931.
2. Bertrand Robert L, Margolin W. Lag Phase Is a Dynamic, Organized, Adaptive, and Evolvable Period That Prepares Bacteria for Cell Division. *Journal of Bacteriology*. 201(7):e00697-18.
3. Bozzaro S. The past, present and future of Dictyostelium as a model system. *The International Journal of Developmental Biology*. 2019;63(8-9-10):321-31.
4. Darwin C. On the Origin of Species by Means of Natural Selection, or the Preservation of Favoured Races in the Struggle for Life. London: Murray; 1859.
5. Fey P, Kowal AS, Gaudet P, Pilcher KE, Chisholm RL. Protocols for growth and development of Dictyostelium discoideum. *Nature Protocols*. 2007;2(6):1307-16.
6. Heaton LLM, Jones NS, Fricker MD. A mechanistic explanation of the transition to simple multicellularity in fungi. *Nature Communications*. 2020;11(1).

7. Igor Segota, Arthur Campello, Brendan H. Rappazzo, Ariana Strandburg-Peshkin, Xiao-Qiao Zhou, Archana Rachakonda, Kayvon Daie, Benjamin Yavitt, Alexander Lussenhop, Sungsu Lee, Kevin Tharratt, Amrish Deshmukh, Elisabeth M. Sebesta, Myron Zhang, Sharon Lau, Sarah Bennedsen, Jared Ginsberg, Timothy Campbell, Chenzheng Wang, Carl Franck. Confirmation and variability of the Allee effect in *Dictyostelium discoideum* cell populations: possible role of paracrine signaling. 2021. In preparation for resubmission to *Physical Biology*.
8. Michael T. Madigan, Paul V. Dunlap, David P. Clark. *Biology of Microorganisms*. 12 ed: Pearson; 2009.
9. Pfeiffer T, Bonhoeffer S. An evolutionary scenario for the transition to undifferentiated multicellularity. *Proceedings of the National Academy of Sciences*. 2003;100(3):1095.
10. Ratcliff WC, Denison RF, Borrello M, Travisano M. Experimental evolution of multicellularity. *Proceedings of the National Academy of Sciences*. 2012;109(5):1595-600.
11. Rolfe MD, Rice CJ, Lucchini S, Pin C, Thompson A, Cameron ADS, et al. Lag Phase Is a Distinct Growth Phase That Prepares Bacteria for Exponential Growth and Involves Transient Metal Accumulation. *Journal of Bacteriology*. 2012;194(3):686-701.
12. Schultz D, Kishony R. Optimization and control in bacterial Lag phase. *BMC Biology*. 2013;11(1):120.
13. Stephens PA, Sutherland WJ, Freckleton RP. What Is the Allee Effect? *Oikos*. 1999;87(1):185.
14. Willensdorfer M. Organism size promotes the evolution of specialized cells in multicellular digital organisms. *Journal of Evolutionary Biology*. 2008;21(1):104-10.

## **Acknowledgments**

I gratefully acknowledge the NSF for providing funding for this research through award number 0552782. I further acknowledge the Cornell Center for Materials Research REU for accepting me to their program and providing the resources and support to take on this project. Finally, I'm indebted to Zijin Huang, Reiley Dorian, Christopher Donohue, and Carl Franck for collecting data, providing the initial coding ideas, proofreading, and general advice.